# Novel Nanostructures of Functional Oxides Synthesized by Thermal Evaporation**

By *Zu Rong Dai*, *Zheng Wei Pan*, and *Zhong L. Wang**

Functional oxides are the fundamentals of smart devices. This article reviews novel nanostructures of functional oxides, including nanobelts, nanowires, nanosheets, and nanodiskettes, that have been synthesized in the authors' laboratory. Among the group of ZnO, SnO_2, In_2O_3, Ga_2O_3, CdO, and PbO_2, which belong to different crystallographic systems and structures, a generic nanobelt structure has been synthesized. The nanobelts are single crystalline and dislocation-free, and their surfaces are atomically flat. The oxides are semiconductors, and have been used for fabrication of nanodevices such as field-effect transistors and gas sensors. Taking SnO_2 and SnO as examples, other types of novel nanostructures are illustrated. Their growth, phase transformation, and stability are discussed. The nanobelts and related nanostructures are a unique group that is likely to have important applications in electronic, optical, sensor, and optoelectronic nanodevices.
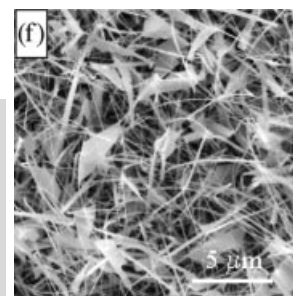
1. Introduction

A widely accepted definition of a nanostructure is a system in which at least one dimension is ≤100 nm,[1] typically including layer-like, wire-like, and particle-like structures. Quantum effects due to size confinement in nanostructures occur when the characteristic size of the object is comparable with the critical lengths (typically 1–10 nm) of the corresponding physical processes, such as the mean free path of electrons, the coherence length, or the screening length.[2] Two-dimensional (2D) quantum wells, one-dimensional (1D) quantum wires, and zero-dimensional (0D) quantum dots are the typical structural forms.

In geometrical morphology, a variety of nanostructures have been fabricated, including tubes,[3–10] cages,[11,12] cylindrical wires[13–20] and rods,[21–23] co-axial[24] and bi-axial cables,[25] ribbons or belts,[26,27] sheets,[28] and diskettes.[29]

Oxides are the basis of smart and functional materials. Synthesis and device fabrication using functional oxides have attracted a lot of attention recently because the physical properties of these oxides can be tuned. Functional oxides have two structural characteristics: cations with mixed valence states,

and anions with deficiencies (vacancies).[30] By varying either or both of these characteristics, the electrical, optical, magnetic, and chemical properties can be tuned, giving the possibility of fabricating smart devices. The structures of functional oxides are very diverse and varied, and there are endless new phenomena and applications. Such unique characteristics make oxides the most diverse class of materials, with properties covering almost all aspects of materials science and physics in areas such as semiconductivity, superconductivity, ferroelectricity, and magnetism.

Since the successful synthesis of semiconducting oxide nanobelts in our laboratory,[26,31] the investigation of oxide nanostructures has attracted considerable attention. Table 1 summarizes almost all of the nanostructures of oxides that have been synthesized up to now. The synthetic approaches can be generally classified into several categories: vapor-phase growth (including thermal evaporation, chemical vapor-phase deposition, metal–organic chemical vapor-phase deposition, arc-discharge, laser ablation, etc.), solution-phase growth, sol–gel, template-based methods, etc. Among these approaches, thermal evaporation is the one most commonly employed in the investigation of oxide nanostructures.

Our recent research has focused on the synthesis and characterization of novel nanostructures of oxide functional materials as well as their applications.

2. Thermal Evaporation

In principle, the thermal evaporation technique is a simple process in which condensed or powder source material(s) is/are

[*] Prof. Z. L. Wang, Dr. Z. R. Dai, Dr. Z. W. Pan[+]
School of Materials Science and Engineering
Georgia Institute of Technology
Atlanta, GA 30332-0245 (USA)
E-mail: zhong.wang@mse.gatech.edu

[+] Present address: Chemical Sciences Division, Oak Ridge National Laboratory, Oak Ridge, TN 37831-6201, USA.

vaporized at an elevated temperature and the resultant vapor phase(s) condense(s) under certain conditions (temperature, pressure, atmosphere, substrate, etc.) to form the desired product(s). The processes are usually conducted in a tube furnace. Figure 1 shows a schematic diagram of the experimental apparatus used in the study presented here. It consists of a horizontal tube furnace (50 cm long), an alumina tube (4 cm diameter, 75 cm long), a rotary pump system, and a gas supply and control system. A viewing window set up at the left end of the alumina tube is used to monitor the growth process. The right end of the alumina tube is connected to the rotary pump. Both ends are sealed by rubber O-rings. The ultimate vacuum for this configuration is $\sim 2 \times 10^{-3}$ torr. The carrier gas enters at the left end of the alumina tube and is pumped out at the right end. The source material(s) is (are) loaded on an alumina boat and positioned at the center of the alumina tube. Several alumina

strip plates (60 mm × 10 mm) were placed downstream, one behind the other, inside the alumina tube (see the enlarged diagram at the bottom of Fig. 1), which acted as substrates for collecting growth products.

The morphology and phase structure of product(s) depend on not only the processing parameters adopted but also source material(s) employed. Different oxides might behave differently during the thermal evaporation. Some reactions may occur upon vaporization of oxides,[113] resulting in different stoichiometric species in the vapor phase(s) from that of the source material(s). For example, solid-state SnO is unstable and tends to decompose into liquid Sn and solid SnO_2 even at a low temperature of 370–400 °C.[113,114] Gaseous SnO is, however, relatively stable, especially at a high temperature (>1300 °C). If the temperature is lower than 1300 °C, the gaseous SnO will spontaneously decompose into liquid Sn and sol-

Zhong Lin Wang received his Ph.D. in Physics from Arizona State University in 1987. He is currently a professor, the Director of the Center for Nanoscience and Nanotechnology, and the Director of the Electron Microscopy Center at Georgia Institute of Technology. Dr. Wang has authored or co-authored four scientific reference and textbooks and 260 journal articles and edited or co-edited six volumes of books on nanotechnology. He has received several prizes, including the 2001 S.T. Li prize for Outstanding Contribution in Nanoscience and Nanotechnology, the 2000 Georgia Tech Faculty Research Award, and the 1999 Burton Medal from the Microscopy Society of America. He is a member of the editorial board of several academic journals. His most recent research focuses on oxide nanobelts and nanowires, in-situ techniques for nanoscale measurements, self-assembled nanostructures, fabrication of nanodevices, and properties of magnetic nanostructures.

Zu Rong Dai received his B.Sc. from Zhejiang University, P. R. China, in 1986, his M.Sc. from the North China Institute of Technology in 1991, and his Ph.D. from the University of Science and Technology, Beijing, in 1996. His Ph.D. research work was carried out at the Beijing Laboratory of Electron Microscopy, Chinese Academy of Sciences. He was a Visiting Scientist at the University of Washington, Seattle, before joining the Georgia Institute of Technology, Atlanta, as a Research Scientist in 1999. His research interests are in the area of nanostructure synthesis and characterization, phase transformation, crystal growth and crystal defects, long- and short-range order of point defects, and interplanetary dust particles.

Zhengwei Pan received his B.S. and M.S. degrees in Materials Science from Shandong University of Technology, P. R. China, in 1990 and 1993, respectively, and his Ph.D. in Materials Science from Northwestern Polytechnic University, P. R. China, in 1997. Before he joined the Georgia Institute of Technology in 2000, he worked at the Institute of Physics, Chinese Academy of Sciences (Beijing, P. R. China), and the City University of Hong Kong. He is currently in the Chemical Sciences Division at the Oak Ridge National Laboratory, Tennessee. His research interests include synthesis, characterization, property measurements, and applications of one-dimensional nanostructures (including nanotubes, nanowires, and nanobelts), nanoparticles, ceramics, and alloys.

Table 1. Summary of oxide nanostructures.

Material	Nanostructure	Fabrication method	Reference
MgO	Rods	Thermal evaporation	[22]
	Wires	Thermal evaporation	[32,33]
	Belts	Chemical vapor deposition	[34]
	Fishbones	Thermal evaporation	[35]
ZnO	Belts	Thermal evaporation	[26,36]
	Wires	Thermal evaporation	[36–41]
	Rods	Thermal evaporation	[36,42]
		Gas reaction	[43]
		Metal-organic vapor-phase epitaxy	[44]
			[45]
		Chemical vapor deposition	[46,47]
	Whiskers	Solution-phase process	[48]
	Tubes	ZnS oxidation	[49,50]
		Solution-phase process	
CdO	Belts	Thermal evaporation	[26]
	Wires	Solution-phase process	[51]
CaO	Rods	Catalytic growth	[52]
SnO	Diskettes	Thermal evaporation	[29]
SnO₂	Belts or ribbons	Thermal evaporation	[26,53–55]
	Wires	Thermal evaporation	[54]
	Tubes	Thermal evaporation	[54]
	Rods	Molten salt synthesis	[56]
		Sol-gel template method	[57]
	Dendrites	Thermal evaporation	Present work
CeO₂	Wires	Thermal evaporation	[58]
	Rods	Template method	[59]
	Whiskers	Laser ablation	[60]
PbO₂	Belts	Thermal evaporation	[31]
PdO₂	Hillocks	Metal oxidation	[61]
TiO₂	Wires	Template sol-gel method	[62,63]
	Rods	Sol-gel template method (Cao)	[57]
	Tubes	Organogel template method	[64]
		Anodic oxidation	[65]
		Solution-phase method	[66]
	Hollow fibers	Template method	[67]
	Helical ribbons	Organogel template method	[64]
	Sheets	Solution-phase method	[68]
(Ti,Ta,V) oxide	Helical tubes	Sol-gel template method	[69]
SiO₂ or SiO_x	Wires	Thermal evaporation	[20,70–76]
	Tubes	Thermal evaporation	[77,78]
		Solution-phase method	[79]
		Template method	[9]
	Helical fibers	Sol-gel template	[80,81]
MnO₂	Wires	Hydrothermal method	[82]
	Rods	Liquid-phase coproportionation	[83]
Mn₃O₄	Wires	Thermal evaporation	[84]
ZrO₂	Tubes	Template method	[85,86]
In₂O₃	Belts	Thermal evaporation	[26]
	Wires	Thermal evaporation	[87]
	Fibers	Thermal evaporation (VLS)	[88]
Sn-In₂O₃ (ITO)	Wires	Electron shower PVD method (VLS)	[89]
Ga₂O₃	Belts or ribbons	Thermal evaporation	[28,90,91]
	Wires	Arc discharge	[92,93]
		Thermal evaporation	[91,94,95]
	Rods	Arc discharge	[96]
	Sheets	Thermal evaporation	[28]
VO_x/V₂O₅	Tubes	Sol-gel template method	[7,9,97,98]
		Solution-phase growth	[99]
Na₂V₃O₇	Tubes	Solid-state reaction	[100,101]
Al₂O₃	Tubes	Template method	[9]
Fe₂O₃	Wires	Thermal evaporation	[102]
	Rods	Aqueous chemical growth	[103]
Cu₂O	Wires	Solution-phase method	[104]
		Electrodeposition	[105]
MoO₃	Tubes	Template method	[9]
	Rods	Template method	[106]
	Tubes	Template method	[106]

Table 1. continued

| Material	Nanostructure	Fabrication method	Reference
MoO₂	Rods	Template method	[106]
RuO₂	Rods	Template method	
	Tubes	Template method	
IrO₂	Rods	Template method	
Sb₂O₅	Rods	Template method	
WO_x	Wires	Etching + thermal oxidation	[107]
WO₃	Rods	Template method	[106]
	Tubes	Template method	[106]
Rare earth (Er, Tm, Yb, Lu) oxides	Tubes	Template method	[108]
BaTiO₃	Rods	Solution-phase method	[109]
		Sol-gel template method	[57]
	Tubes	Sol-gel template method	[110]
SrTiO₃	Rods	Solution-phase method	[109]
PbTiO₃	Tubes	Sol-gel template method	[110]
Sr₂Nb₂O₇	Rods	Sol-gel template	[57]
PZT	Rods	Sol-gel template	[57,111]
Bi₂Sr₂ CaCuO₈₊δ	Whiskers	Vapor-phase method (VLS)	[112]
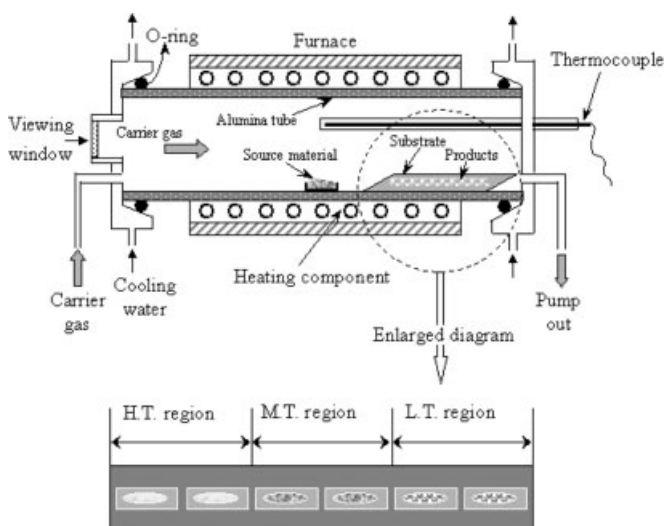
Fig. 1. Schematic diagram of experimental apparatus for growth of oxide nanostructures. An enlarged diagram of the substrate enclosed in the dotted-line circle is shown at the bottom, where several alumina strip plates (60 mm × 10 mm) were placed downstream one behind the other inside an alumina boat. The temperature decreases gradually from left to right, giving three temperature regions (high (H.T.), medium (M.T.), and low temperature (L.T.)), in which the product(s) may have different morphology or crystal structure.

id SnO₂ during the process of lowering the temperature. SiO also has a similar behavior.[115] In contrast, evaporating solid SnO₂ does not directly lead to SnO₂ in the vapor phase, but SnO instead, because the SnO₂ will decompose into gaseous SnO and O₂ at the elevated temperature.[116,117] It is therefore very important to understand the characteristics of the source material(s) upon vaporization to achieve controlled growth of desired nanostructures.

There are several processing parameters, such as temperature, pressure, carrier gas (including gas species and its flow rate), substrate, and evaporation time period, that can be controlled and need to be selected properly before and/or during the thermal evaporation. The choice of source temperature

mainly depends on volatility of the source material(s). Usually, it is slightly lower than the melting point of the source material. The pressure is determined according to the evaporation rate or vapor pressure of source material(s). The substrate temperature usually drops as a function of the distance from the position of source material(s): the greater the distance, the lower the substrate temperature. Of course, the temperature field in the furnace tube can be changed and controlled by introducing a cold finger/plate or by using a multiple-zone furnace. Selecting a proper evaporation time is also important because it influences not only the amount but also the size and the morphology of the product(s). It is also noted that the thermal evaporation process is very sensitive to the concentration of oxygen in the growth system.[29] Oxygen influences not only the volatility of the source material(s) and the stoichiometry of the vapor phase but also formation of product(s). In the present study, after the alumina tube had been evacuated to $\sim 2 \times 10^{-3}$ torr, thermal evaporation was conducted at a certain temperature (Table 2) for 2 h, under a pressure of 200–600 torr and an Ar carrier gas flow of 50 sccm (standard cubic centimeters per minute). In the next few sections, after discussion of the formation of the various Sn–O nanostructures as an example, we will sketch a possible picture of how the processing parameters influence the morphology and phase structures of oxide nanostructures.

3. Nanostructures of Oxides

3.1. Nanobelts

Nanobelts or nanoribbons have been successfully synthesized for a series of oxides with different valence states and different crystal structures, including ZnO, SnO_2, In_2O_3, CdO, Ga_2O_3,[26] and PbO_2[31] (Fig. 2). With the exception of PbO_2, these are transparent conducting oxide (TCO) materials, and have wide applications in architectural glass, gas sensors, flat
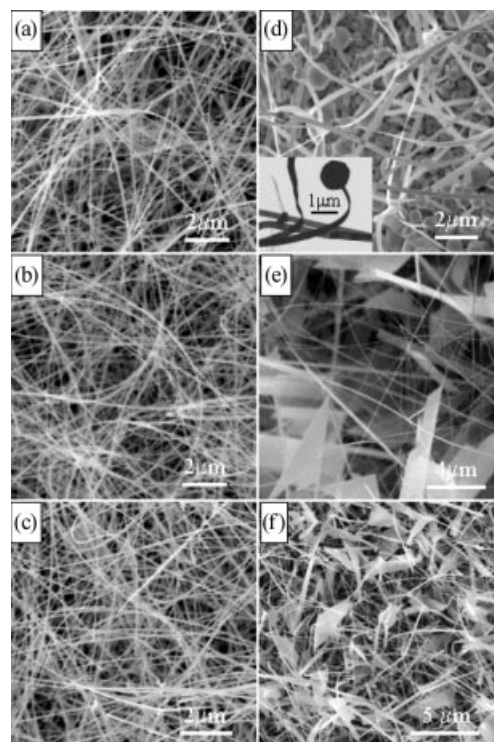

Fig. 2. Typical SEM images of samples of a) SnO_2, b) ZnO, c) In_2O_3, d) PbO_2, e) CdO, and f) Ga_2O_3. Inset in (d) is a TEM image of a PbO_2 nanobelt that has a facet Pb head at one of its ends. All of the products were collected from the substrates in the high-temperature region.

panel displays, advanced optoelectronic devices, etc.; the current worldwide annual revenue is 18 billion dollars.[118] The PbO_2 nanobelts are unique in that each belt has a faceted Pb head located at one of its ends (inset in Fig. 2d).

Figure 3a is a transmission electron microscopy (TEM) image of the SnO_2 nanobelts that were synthesized at 1050 °C using SnO powders (purity 99.9 %, melting point 1080 °C). The same nanostructure can also be made at 1350 °C from SnO_2

Table 2. Synthesis conditions and morphology characteristics of oxide nanostructures.

Nano-structure	Source materials	Evaporation temperature [°C]	Pressure [torr]	Substrate temperature [°C]	Length [μm]	Width or diameter [nm]	Width-to-thickness ratio
ZnO belt	ZnO	1400	200–300	800–1100	>500	50–300	5–10
t-SnO$_2$ belt [a]	SnO	1050	200–300	800–950	>500	30–200	5–10
	SnO$_2$	1350					
In$_2$O$_3$ belt	In$_2$O$_3$	1400	200–300	800–1100	50–300	50–150	5–10
CdO belt	CdO	1000	200–300	700–800	<100	100–500	>10
CdO sheet	CdO	1000	200–300	700–800	5–10 μm	5–10 μm	20–60 nm (thickness)
Ga$_2$O$_3$ belt	Ga$_2$O$_3$	1400	200–300	800–1100	50–500	20–100	5–10
	GaN	950		700–850			
Ga$_2$O$_3$ sheet	GaN	950	200–300	700–850	5–10 μm	5–10 μm	20–60 nm (thickness)
PbO$_2$ belt	PbO	950	200–300	600–800	50–200	50–300	5–10
t-SnO$_2$ wire [a]	SnO	1050	250–700	25–40	>500	30–100	2–5
o-SnO$_2$ wire [b]	Sn+SnO	1050	200	25–40	>500	100–600	2–3
SnO diskette	SnO	1050	500–600	200–400		100 nm–10 μm	15
	SnO$_2$	1350					

[a] t-SnO$_2$ represents rutile structured SnO$_2$. [b] o-SnO$_2$ represents orthorhombic structured SnO$_2$.
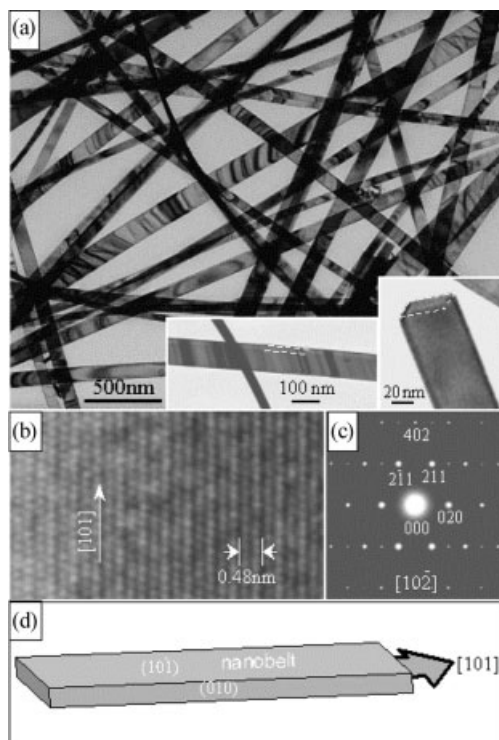
Fig. 3. a) TEM bright-field image of SnO_2 nanobelts. The insets show the geometrical shape of the nanobelts. b,c) HRTEM image and corresponding electron diffraction pattern, respectively, from a nanobelt. d) Schematic diagram of the geometrical configuration of a nanobelt. The sample was synthesized using SnO powders evaporated under 200–300 torr (argon) at 1050 °C. The sample was collected from the substrate in the high-temperature region of 800–950 °C.

powders (purity 99.9 %, melting point 1630 °C). The nanobelts were collected in the high-temperature region of 800–950 °C. The insets in Figure 3a are enlarged TEM images of the nanobelts, in which the geometrical configuration of the nanobelts is clearly displayed; a rectangular cross section with a typical width-to-thickness ratio of ~5 to 10 is shown. The length of SnO_2 nanobelts is up to the order of millimeters. Electron diffraction (Fig. 3c) and high-resolution TEM (HRTEM) images (Fig. 3b) reveal that an individual nanobelt is a single crystal of the rutile structure with lattice constants

$a = 4.722$ Å and $c = 3.184$ Å,[119] and SnO_2 nanobelts grow along the [101] crystal direction and terminate in $\pm(010)$ and $\pm(10\bar{1})$ crystallographic facets (Fig. 3d). A similar morphology is also adopted by other oxide nanobelts. The corresponding processing parameters and structural features are listed in Tables 2 and 3.

3.2. Nanowires

When a layered Sn foil/SnO reactant mixture was used as the source material instead of the SnO powders and a cold plate was introduced into the system, rutile-structured SnO_2 nanowires were obtained (Fig. 4a).[54] The crystallographic configuration of the SnO_2 nanowires is similar to that of the SnO_2 nanobelts described above. They also have a rectangular cross section enclosed by $\pm(010)$ and $\pm(10\bar{1})$ facet planes, but the width-to-thickness ratio is 2–5, smaller than that for SnO_2 nanobelts (5–10). The growth direction of the SnO_2 nanowires is also parallel to the [101] crystal direction (Fig. 4b). As regards morphology, the diameter of the nanowires varies from wire to wire in a broad range, and SnO_2 nanowires are always straight, even very thin ones with a diameter of several tens of nanometers. The HRTEM image (Fig. 4b) and corresponding fast Fourier transform (FFT) (inset in Fig. 4b) are the same as those shown in Figures 3b and 3c, respectively.

Besides the normal rutile-structured SnO_2 nanowires, it is found that some SnO_2 nanowires have a different crystal structure. Shown in Figure 4c is a low magnification TEM image of a SnO_2 nanowire and Figure 4d is the corresponding HRTEM image. The inset in Figure 4d is a FFT of the HRTEM image (Fig. 4d). Evidently, both the HRTEM image (Fig. 4d) and the FFT pattern (inset in Fig. 4d) differ from those for rutile-structured SnO_2 nanowires (Fig. 4b and inset in Fig. 4b). Some extra-weak reflections are clearly seen in the FFT pattern inserted in Figure 4d, in comparison to the FFT pattern inserted in Figure 4b. The crystal structure of the nanowire (Figs. 4c,d) matches the orthorhombic-structured SnO_2, having lattice parameters $a = 0.4714$ nm, $b = 0.5727$ nm, and $c = 0.5214$ nm, which has been found to be formed under very high pressure

Table 3. Crystallographic geometry of oxide nanostructures.

Nanostructures	Crystal structure	Growth direction	Top surface	Side surface
ZnO belt	Wurtzite	[0001] or [01$\bar{1}$0]	$\pm(2\bar{1}\bar{1}0)$ or $\pm(2\bar{1}\bar{1}0)$	$\pm(01\bar{1}0)$ or $\pm(0001)$
Ga_2O_3 belt	Monoclinic	[001] or [010]	$\pm(100)$ or $\pm(100)$	$\pm(010)$ or $\pm(10\bar{1})$
Ga_2O_3 sheet	Monoclinic	[101] (normal)	$\pm(100)$	$\pm(010)$, $\pm(10\bar{1})$ & $\pm(21\bar{2})$
t-SnO_2 belt	Rutile	[101]	$\pm(10\bar{1})$	$\pm(010)$
t-SnO_2 wire	Rutile	[101]	$\pm(10\bar{1})$	$\pm(010)$
o-SnO_2 wire	Orthorhombic	[010]	$\pm(100)$	$\pm(001)$
In_2O_3 belt	C-Rare earth	[001]	$\pm(100)$	$\pm(010)$
CdO belt	NaCl	[001]	$\pm(100)$	$\pm(010)$
CdO sheet	NaCl	<100> (normal)	$\pm\{100\}$	$\pm\{010\}$ & $\pm\{011\}$
PbO_2 belt	Rutile	[010]	$\pm(201)$	$\pm(10\bar{1})$
SnO diskette	Tetragonal	$\pm$<100> & $\pm$<110> [a]	$\pm(001)$	~ $\pm\{100\}$ & $\pm\{110\}$ [a]

[a] For the case that the diameter of the SnO diskette is smaller than 1 μm. "~" means that the corresponding crystal plane is a central tangent plane of an arc side. For the case that the diameter is larger than 1 μm, the diskette has a solid wheel shape with a grooved rim.
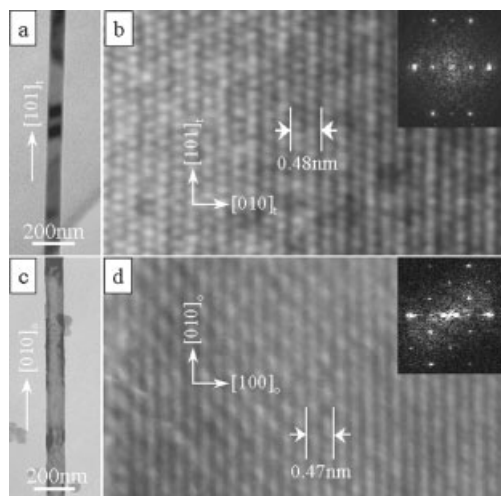
Fig. 4. a) Low magnification TEM image of a rutile-structured SnO_2 nanowire. b) HRTEM image corresponding to the SnO_2 nanowire shown in (a). c) Low magnification TEM image of an orthorhombic-structured SnO_2 nanowire. d) HRTEM image corresponding to the SnO_2 nanowire shown in (c). The insets are FFTs of the corresponding HRTEM images. The sample was made using a layered Sn foil/SnO reactant mixture. The furnace temperature was 1050 °C and the chamber pressure 200 torr (argon). The sample was collected from the cold plate region (25–60 °C).

$(156 \text{ kbar} \approx 1.2 \times 10^8 \text{ torr})$.[120] Combining the electron diffraction and HRTEM image analyses indicates that the orthorhombic SnO_2 can be regarded as a superstructure of rutile-structured SnO_2, and the orientation relationship between the orthorhombic SnO_2 and the tetragonal (rutile) SnO_2 is determined to be $[001]_o \| [10\bar{2}]_t$ and $(100)_o \| (010)_t$, where the subscripts o and t represent the orthorhombic SnO_2 phase and the rutile-structured SnO_2 phase, respectively.[54] Assuming the cross-sectional shape of the nanowire is rectangular, the orthorhombic SnO_2 nanowire is enclosed by $\pm(100)_o$ and $\pm(001)_o$, and its growth direction is along the $[010]_o$ crystal direction.

3.3. Sandwiched Nanoribbons

Another type of wire-like nanostructure is shown in Figure 5a, in which the nanostructure consists of two side layers of a thickness about 20 nm and a core layer with a width ~120 nm. Considering the contrast over the length and the chemical imaging results, the wire-like nanostructure has a rectangular cross section with a smaller aspect ratio than that of the nanobelts. It is therefore called a sandwiched nanoribbon to distinguish it from the nanobelts. Although parts of the side layers are missing, the nanoribbon has a uniform width over its entire length in general. The composition of the sandwiched nanoribbon determined by X-ray energy-dispersive spectroscopy (EDS) also approaches SnO_2. Electron micro-diffraction patterns were recorded from the core layer (Fig. 5b) and side layer (Fig. 5c) separately. Evidently, the reflections corresponding to the rutile-structured SnO_2 are very strong in the micro-diffraction pattern taken from the center of the core layer (Fig. 5b), although weak reflections of orthorhombic SnO_2 can be identified. The micro-diffraction pattern from the
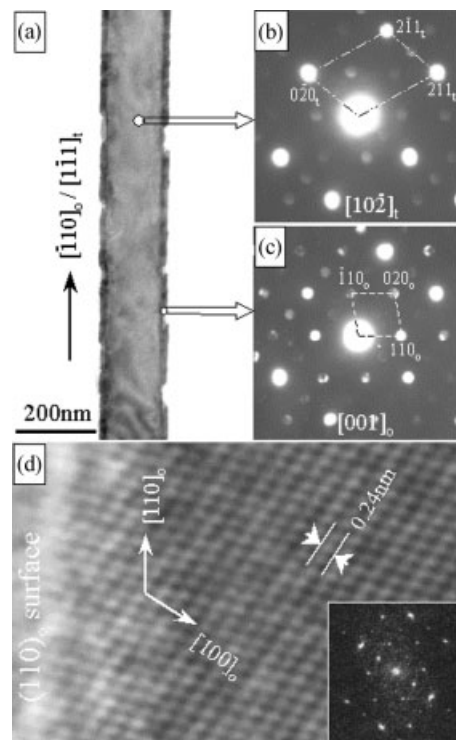

Fig. 5. a) TEM image of a sandwiched nanoribbon. b,c) Microdiffraction patterns taken from the center and edge of the nanoribbon, respectively. The sample was made using a layered Sn foil/SnO reactant mixture. The furnace temperature was 1050 °C and argon pressure 250–700 torr. The sample was collected from the cold plate. d) HRTEM image of the edge area of the sandwiched nanoribbon shown in (a). Inset is the corresponding FFT.

side layer (Fig. 5c), however, displays a stronger diffraction feature of orthorhombic SnO_2.[120] This implies that the core layer is likely to have the rutile structure while the side layers adopt the orthorhombic structure predominantly. The superlattice reflection observed in the pattern recorded from the center of the nanoribbon may come from the top and bottom surface layers, which are dominated by orthorhombic structure. A HRTEM image recorded near the edge layer is displayed in Figure 5d, and the corresponding FFT is given in the inset, which verifies the fact that the orthorhombic structured SnO_2 is formed in the side layer. The surface of the SnO_2 nanoribbon edge is not flat on the atomic sale, as indicated by the HRTEM image (Fig. 6). The orthorhombic SnO_2 and the normal rutile
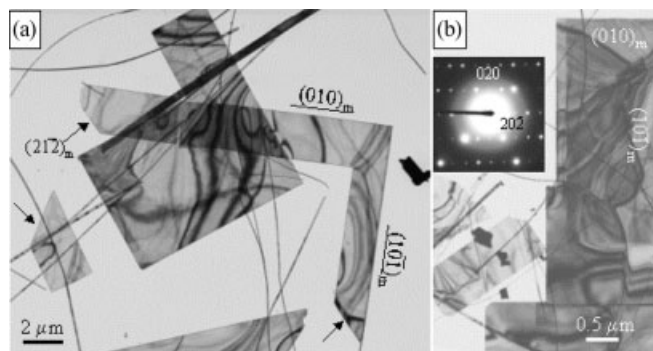

Fig. 6. a,b) Low-magnification TEM images of Ga_2O_3 nanosheets. The inset in (b) is the corresponding electron diffraction pattern recorded from the large nanosheet [28].

SnO_2 are coherent with an orientation relationship of $[001]_o \| [10\bar{2}]_t$ and $(100)_o \| (010)_t$, which is the same as that deduced from the case of the orthorhombic SnO_2 nanowires presented in Section 3.2. The sandwiched SnO_2 nanoribbons, however, are enclosed by $\pm(110)_o/\pm(231)_t$ and $\pm(001)_o/\pm(10\bar{1})_t$, and their growth directions are parallel to $[\bar{1}10]_o/[6\bar{5}3]_t$.[54]

3.4. Nanosheets

Some sheet-like nanostructures can be identified from the scanning electron microscopy (SEM) images of samples of CdO (Fig. 2e) and Ga_2O_3 (Fig. 2f). Shown in Figures 6a and 6b and the inset in Figure 6b are TEM images and the corresponding electron diffraction pattern of β-Ga_2O_3 nanosheets, which have a monoclinic structure (space group $C2/m$) with lattice constants $a = 12.23$ Å, $b = 3.04$ Å, $c = 5.80$ Å Å, and $\beta = 103.7°$.[121] Nanosheets have some straight edges with corners of specific angles, typically 45° and 90° (Fig. 6a). The inserted electron diffraction pattern in Figure 6b is to the [101] crystal zone of β-Ga_2O_3. The two perpendicular planes result in the rectangular and L-shaped structures (Fig. 6a). Beside the $\pm(0\bar{1}0)$ and the $\pm(10\bar{1})$ facets, a third type of plane making an ~45° angle with the two sides, as indicated by arrows in Figure 6a, is also observed. This type of plane is identified as the $(21\bar{2})$ plane from the electron diffraction pattern. The top and bottom surfaces are also the $\pm(100)$ crystal planes of β-Ga_2O_3. Based on our SEM observation, the thickness of the nanoribbons and nanosheets is 20–60 nm.

3.5. Nanodiskettes

Figure 7a is a SEM image showing the diskette-like product that was made using either SnO or SnO_2 powders under a higher pressure (500–600 torr compared with 200 torr used for the nanobelt synthesis). The product was collected in the low-temperature region of 200–400 °C. The typical diameter of the diskettes in Figure 2 is 8–10 μm. The thickness of the diskettes is several tens to several hundreds of nanometers, according to the dimension of the corresponding diameter. The aspect ratio of diameter-to-thickness is about 15. Electron diffraction and X-ray diffraction analyses[29] have determined that each diskette is a single crystal having the tetragonal SnO structure ($P4/nmm$, $a = 3.796$ Å and $c = 4.816$ Å),[122] of which the a- and b-axes are equivalent, but not the c-axis. The normal direction of the diskette is parallel to [001]. The formation of a circular contour is likely to lower the surface energy.

Two main types of SnO diskettes (type I and type II) have been identified based on morphology. The type I SnO diskettes (Fig. 7b,c) possess a uniform thickness and flat surfaces. A perfect circular contour is adopted by the type I SnO diskettes, whose diameters are larger than 1 μm. The side view of a type I SnO diskette (Fig. 7c) reveals that its geometrical shape is actually a solid wheel with a groove around its periphery. It
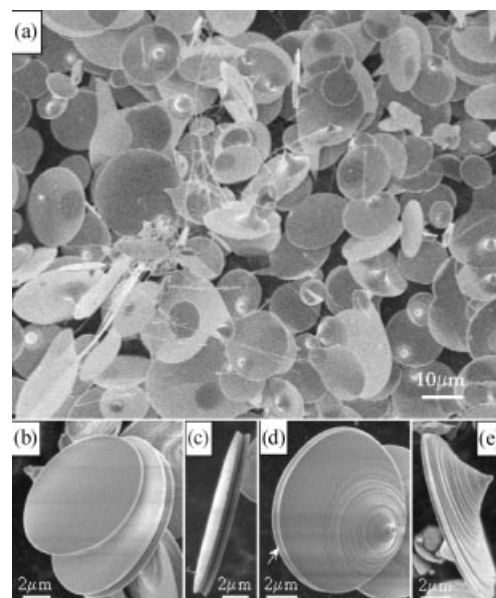

Fig. 7. a) SEM image of tin oxide diskettes. b,c) SEM images showing morphologies of type I tin oxide diskettes with flat surfaces. d,e) SEM images showing morphologies of type II tin oxide diskettes with the growth features of terraces and spiral steps. The sample was made using SnO powders under 500–600 torr (argon) at 1050 °C and collected from the low temperature region of 200–400 °C.

appears that two wedged-rim diskettes stick together face-to-face. Figures 7d and 7e show SEM images of type II SnO diskettes, whose top surfaces are not flat. Instead, terraces and spiral steps can be identified, resulting in the formation of a cone-like peak on the top surface of the SnO diskettes. The center of the cone is not necessarily located at the center of the diskette. The apexes of cone peaks are globules that have been identified to be Sn rich. The grooved edge is also consistently observed for type II SnO diskettes (for example as indicated by the arrowhead in Fig. 7d).

The formation of the SnO diskettes likely follows a solidification (liquid–solid) process.[29] During the growth of the SnO diskettes, as the SnO vapor moves with the carrier gas (Ar) into the low-temperature region, the SnO vapors may first become super-cold liquid SnO droplets, provided that the flow of the carrier gas is very slow and the chamber pressure is relatively high, which is true in our case. Then the super-cold SnO droplets condense onto either the alumina substrate or the surfaces of the SnO_2 nanobelts carried over by the carrier gas from the high-temperature region, resulting in nucleation and growth by continuous incorporation of the incoming droplets. Preference for diskettes with a large (001) surface is possibly governed by crystal structure and surface energy. If the (001) surfaces of the crystallized SnO are constantly kept clean and the arriving droplets can constantly wet and cover the entire condensed (001) surface during growth, a type I SnO diskette will form. If some impurity generated during the growth is deposited onto the diskettes around which the cone peak will form, the formation of the type II SnO diskette results. Another possibility is that liquid Sn droplets guide growth of the SnO diskettes. The spiral growth feature of the cone peak is similar to that of a screw-dislocation-guided growth process,[123]

but a contribution from the vapor–liquid–solid process still cannot be completely ruled out due to the presence of the Sn globules at the ends of cone-like peaks.

3.6. Blocks and Nanodendrites

The substrate temperature has significant influence on the morphology and phase structure of oxide nanostructures. In the low-temperature region, the form of the product(s) becomes more complex. Different products may form in the same temperature region during different growth periods. The SnO diskettes are always found together with SnO_2 nanobelts and most of them are suspended on the nanobelts. Underneath the SnO diskettes and at the bottom of the substrate, a large quantity of block-like SnO product was made (Fig. 8). The SnO blocks are of regular geometrical shapes (Figs. 9a–c). The characteristic size of the SnO blocks is 10–50 μm. Some of the

blocks can self-assemble one on top of another (Fig. 9b). It is very interesting that some slot-like defects are symmetrically distributed in the SnO blocks (Figs. 9a,b).

Elevating the source temperature to 1100 °C (for the SnO powders) and increasing the pressure to 500–600 torr, another form of product was obtained in the low-temperature region, which covers the SnO diskettes and displays a dendrite-like structure (Figs. 10a,b). The main branch is typically 150–250 nm in diameter. The diameter of the sub-branches is, how-
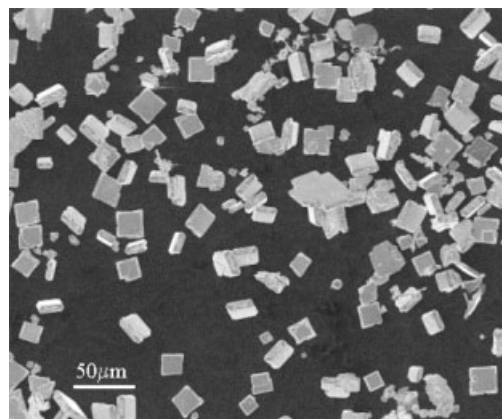

Fig. 8. SEM image of SnO blocks. The sample was made using SnO powders under 500–600 torr (argon) at 1050 °C and collected from the low-temperature region of 200–400 °C.
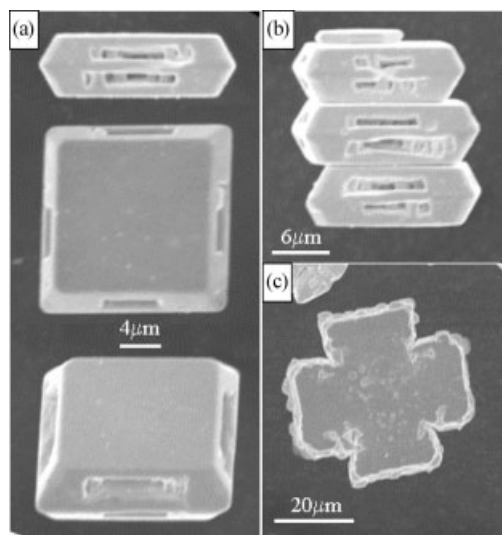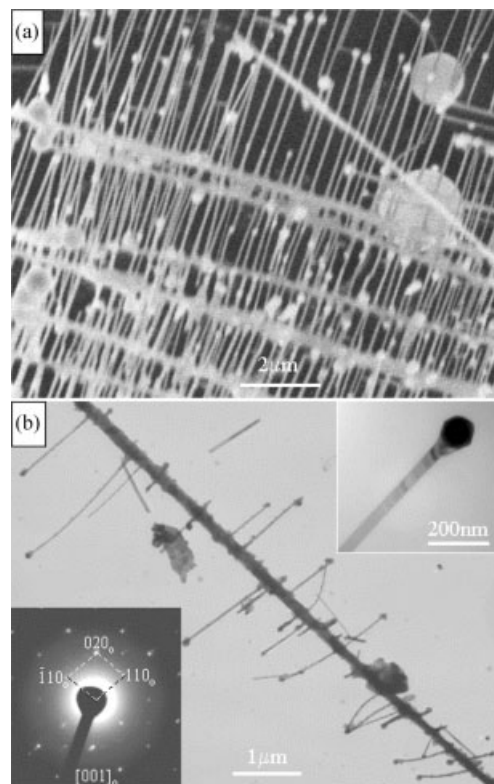

Fig. 9. a) SEM images showing side view, front view, and perspective of one block. b) SEM image of self-stacked SnO blocks. c) SEM image of a cross-like block.

Fig. 10. a) SEM image of SnO_2 dendrites. b) TEM image of a SnO_2 dendrite. Bottom left inset: selected area electron diffraction pattern from a side branch wire (upper right inset). The sample was made using SnO powders under 500–600 torr (argon) at 1050 °C and collected from the low-temperature region of 200–400 °C.

ever, only 30–50 nm. The growth of the sub-branches is very nearly perpendicular to the main branch, and each sub-branch has a ball located at or near its tip (inset in upper right corner of Fig. 10b). EDS analysis indicates that the ball is Sn rich. Such a growth feature implies that the nanodendrites are likely formed by the VLS (vapor–liquid–solid) mechanism,[124] in which the Sn-rich ball serves as the "catalyst" to guide the branches, especially the sub-branches, to grow along a certain crystallographic direction. Figure 10b shows a TEM image of a nanodendrite and the corresponding electron diffraction pattern (bottom left inset). It has been determined that the nanodendrites have the orthorhombic SnO_2 crystal structure, and the main branch and sub-branches grow along the $[\bar{1}10]$ and $\pm[110]$ crystallographic directions, respectively, which are equivalent in crystallography for the orthorhombic crystal lattice.

4. Crystal Defects of Oxide Nanostructures

Generally speaking, nanostructures of oxides have very good crystallinity that is comparable to bulk materials. Oxygen vacancy point defects are always found in the oxide nanostructures, especially for the nanostructures formed in the low-temperature region, such as SnO nanodiskettes and nanodendrites. Besides these point defects, stacking faults and twinning are often observed in oxide nanobelts. Domain boundaries and dislocations were also found in sandwiched SnO_2 nanoribbons.[54]

Figure 11a is a TEM image of a ZnO nanobelt, where a plane defect is located at the center of the nanobelt and extends throughout the entire nanowire. An enlarged HRTEM
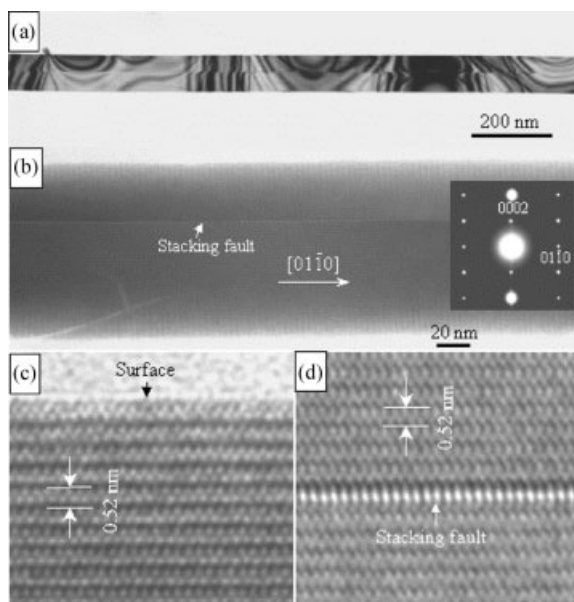

Fig. 11. a) Low-magnification TEM image of ZnO nanobelt with a stacking fault. b) HRTEM image and the corresponding electron diffraction pattern (inset). c) Enlarged HRTEM image showing a side surface of ZnO nanobelt. d) Enlarged HRTEM image around the stacking fault.

image (Fig. 11d) shows that the defect is a stacking fault. For the ZnO wurtzite structure, the stacking fault plane is (0001), which can be determined from the electron diffraction pattern shown as the inset in Figure 11b. Usually, the oxide nanobelts have a very clear and atomically flat surface (Fig. 11c), without any amorphous coating layer on their surfaces. This is a unique characteristic superior to that of metal and semiconducting nanowires, whose surfaces are always covered with an amorphous oxide layer that may affect their electric contact properties.

Figure 12a shows a TEM image of a rutile-structured SnO_2 nanowire with a single twin structure. The corresponding selected area diffraction pattern is shown in Figure 12c, where the reflections indexed with a subscript "T" are from the twin part relative to the matrix part whose reflection indexes are marked without a subscript. The zone axis of the diffraction pattern is [010]. The twinning plane is determined to be (10$\bar{1}$) and the twinning direction is [101], which is parallel to the growth direction of the SnO_2 nanowire. The twin can be regarded as being formed by one part of the crystal (twin part)
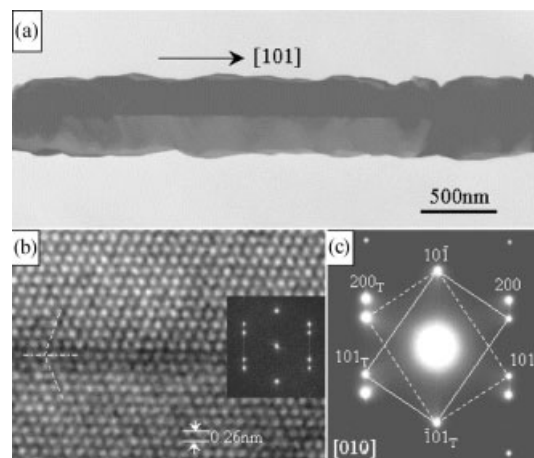

Fig. 12. a) TEM image of a SnO_2 nanowire with twin structure, b) HRTEM image of the twin, where the inset is the corresponding FFT of the image. c) Electron diffraction pattern from the nanowire shown in (a). The sample was made by vaporizing SnO powder at a furnace temperature of 1050 °C and a chamber pressure (argon) of 250 torr. The sample was collected from a cold plate region [54].

that rotates 180° around the normal direction of the (10$\bar{1}$) crystal plane while the other part of the crystal (matrix part) retains the original orientation. Shown in Figure 12b is a HRTEM image around the twin boundary. The twin boundary is completely coherent, and there is no relative displacement. The inset is a FFT of the HRTEM image, which is consistent with the experimental electron diffraction pattern given in Figure 12c.

5. Instability of Oxide Nanostructures

5.1. Electron Beam-Induced Phase Transformation

As pointed out previously, the presence of oxygen vacancies is an important characteristic for tuning the properties of oxide functional materials. On the other hand, due to the presence of oxygen vacancies, some oxide nanostructures are sensitive to electron beam irradiation. Electron beam-stimulated phase transformation in β-PbO_2 nanobelts is an example.[31] The PbO_2 nanobelts have a rectangular cross section and are enclosed by top surfaces ±(201) and side surfaces ±(10$\bar{1}$); their growth direction is parallel to [010] (Fig. 13a). Figure 13b is a dark-field TEM image of a PbO_2 nanobelt, which was taken after the nanobelt had been illuminated by an electron beam for a certain period of time. A mottled contrast is displayed over the nanobelt (Fig. 13b), implying occurrence of some precipitation under the electron beam irradiation. Shown in Figure 13d is a corresponding electron diffraction pattern, in which two sets of patterns can be identified. One is from tetragonal PbO_2 ($P4/nmm$, $a = 4.961$ Å and $c = 3.385$ Å),[125] which is the original phase synthesized. The thick-line frame marked in the pattern (Fig. 13d) represents the basic unit of the diffraction pattern corresponding to the tetragonal PbO_2; its reflections are indexed with a subscript "2". The other pattern is determined to be the red tetragonal PbO phase ($P4/nmm$,
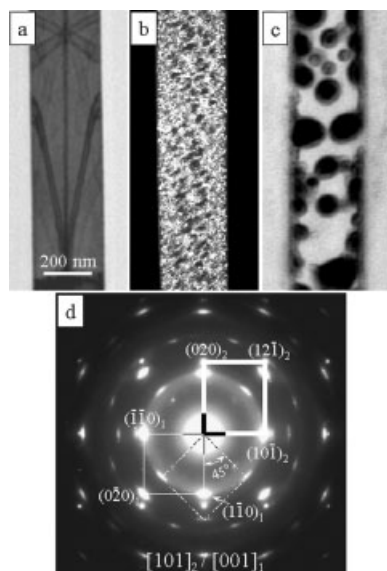
Fig. 13. a) A bright-field TEM image of an individual PbO$_2$ nanobelt. b) Dark-field TEM image of the PbO$_2$ nanobelt subjected to electron beam irradiation, where the mottled contrast indicates occurrence of precipitation. c) Bright-field TEM image of the PbO$_2$ nanobelt undergoing long time irradiation, in which PbO$_2$ has decomposed into metal Pb. d) Electron diffraction pattern of the nanobelt shown in (b), displaying the phase transformation from PbO$_2$ to PbO [31].

Fig. 14. XRD spectra of SnO powders (a), SnO diskettes (b), SnO diskettes annealed at 500 °C for 2 h in oxygen atmosphere (c), SnO$_2$ powders (d), and SnO diskettes annealed at 700 °C for 2.5 h in oxygen atmosphere (e) [29].

$a = 3.961$ Å and $c = 5.011$ Å),[126] as marked by a thin-line frame; the corresponding reflections are indexed with a subscript "1". This indicates that the original PbO$_2$ phase transforms into a PbO phase upon irradiation by an electron beam under high vacuum due to pumping off of the O$_2$ decomposed from the PbO$_2$. The dominant orientation relationship between the PbO$_2$ and the PbO is determined to be $(010)_2 \| (100)_1$ and $[101]_2 \| [001]_1$. Another preferred orientation of the PbO phase precipitation is that as indicated by a dashed-line frame, which is rotated by 45° relative to the former case. Upon further illumination of the nanobelt, the PbO is completely reduced to metal Pb, as shown in Figure 13c.

5.2. Thermal Decomposition of an Unstable Phase

Although the SnO nanodiskette is a very interesting structural form, the tetragonal SnO phase is a thermodynamically unstable phase.[114] It may decompose into SnO$_2$ and Sn even at the relatively low temperature of 370–400 °C.[113] In order to obtain the stable rutile-structured SnO$_2$, the as-synthesized SnO diskettes were annealed at different temperatures in an oxygen atmosphere. Figure 14 shows five X-ray diffraction (XRD) spectra, of which spectra a and e are for standard SnO and SnO$_2$ powders, respectively, which are used as the reference spectra for the following analysis. The crystal structure of SnO powder is determined to be tetragonal ($P4/nmm$) with lattice parameters $a = 3.796$ Å and $c = 4.816$ Å.[122] The SnO$_2$ powders are of the rutile structure ($P4_2/mnm$) with lattice parameters $a = 4.737$ Å and $c = 3.185$ Å.[119] Most of the peaks in the XRD spectrum from the as-synthesized SnO diskettes (spectrum b) fit to the tetragonal SnO, but some extra peaks are also

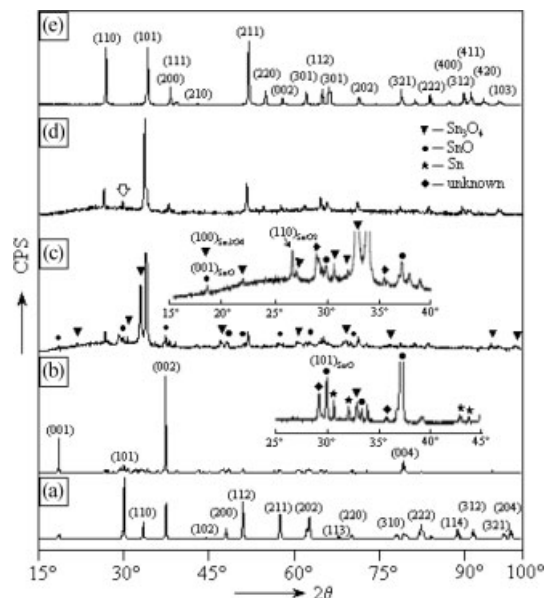identified, which come from some other minor phase(s). The range of spectrum b from 25° to 45° is shown enlarged. Besides the peaks from SnO, marked by black dots, four peaks characteristic of metal Sn (β-Sn) ($I4_1/amd$, $a = 5.832$ Å and $c = 3.182$ Å)[127] are identified (marked by stars), which are indexed as the (200), (101), (220), and (211) reflections from Sn. The Sn peaks are likely from the globular tips that are observed to be associated with the SnO diskettes. The unmarked peaks are from the remaining SnO$_2$ nanobelts because the SnO diskettes always co-exist with SnO$_2$ nanobelts. In fact, a few SnO$_2$ nanobelts can be identified in the SEM image shown in Figure 7a.

The peak marked by an inverted triangle is probably from Sn$_3$O$_4$ phase, as discussed later. Two more weak peaks are still left, located at 28.6° and 35.8° and marked by diamonds, which might come from some other intermediate phase(s). After the sample has been annealed at 500 °C for 2 h in an oxygen atmosphere, the XRD spectrum (spectrum c) has dramatically changed in comparison to spectrum b. The intensity of the SnO peaks marked by black dots significantly decreases and the rutile-structured SnO$_2$ phase is identified; its diffraction peaks are unlabeled in the figure. In addition, some other peaks, as marked by inverted triangles, are clearly distinguished, which are determined to match the Sn$_3$O$_4$ phase, which has a triclinic lattice structure with lattice parameters $a = 4.86$ Å, $b = 5.88$ Å, $c = 8.20$ Å, $\alpha = 93.00°$, $\beta = 93.35°$, and $\gamma = 91.00°$.[128] The details can be found in the enlarged part of spectrum c, where all main peaks of the Sn$_3$O$_4$ phase can be identified. At this stage, however, no peak of metal Sn can be found, indicating that the metal Sn identified originally in the as-synthesized sample has been oxidized during the annealing. Similar to that found in the enlarged part of spectrum b, the two peaks located at 28.6° and 35.8° are also identified in spectrum c, as marked by black diamonds. When the annealing temperature is increased to

700 °C, almost pure rutile-structured SnO_2 is obtained (spectrum d) in comparison to the standard spectrum from SnO_2 powders as given as spectrum e. Only one extra peak with distinguishable intensity, as marked by an open arrowhead, is found, at $2\theta = 29.8°$. The position is consistent with that of the (101) peak of tetragonal SnO, indicating that a small amount of SnO might still remain. On the other hand, a certain texture structure still exists in the SnO_2 product since the intensity of the (101) peak is abnormally strong compared to that of the SnO_2 powders' spectrum (e).

It is therefore evident that the phase transformation from SnO to SnO_2 in an oxygen atmosphere is not a simple one-step process of oxidization but occurs via intermediate reactions. The solid-state SnO is thermodynamically unstable with respect to β-Sn and SnO_2.[129] The decomposition reaction $2SnO(s) \rightarrow SnO_2(s) + Sn(l)$ was reported to occur starting at as low as 370 °C,[113] where "s" and "l" represent solid state and liquid state, respectively. Some intermediate oxide phases such as Sn_3O_4,[128] Sn_2O_3,[130] and Sn_5O_6[131] were also reported to exist. Especially, Sn_3O_4 was found to be formed by decomposition of SnO in a nitrogen atmosphere.[128] In the present study, however, the SnO diskettes were annealed in an oxygen atmosphere, and the Sn_3O_4 phase has also been clearly identified to co-exist with SnO_2, but with the absence of Sn in the sample after annealing at 500 °C for 2 h. The Sn_3O_4 phase completely disappears when the sample is continuously annealed at 700 °C for 2.5 h. Based on this evidence, the following reactions are likely to be responsible for the SnO → SnO_2 phase transformation in an oxygen atmosphere:

$$4SnO(s) \rightarrow Sn_3O_4(s) + Sn(l) \tag{1}$$

$$Sn_3O_4 \rightarrow 2SnO_2(s) + Sn(l) \tag{2}$$

$$Sn(l) + O_2 \rightarrow SnO_2(s) \tag{3}$$

Thus the phase transformation from SnO to SnO_2 is two processes of decomposition and oxidization. The decomposition process consists of the two-step reaction of Equations 1 and 2, which is similar to that of the decomposition of SnO occurring in a nitrogen atmosphere.[128] The oxidization process (Eq. 3) occurs simultaneously with the decomposition process.

5.3. Phase Transformation of Orthorhombic-Structured SnO_2 to Rutile-Structured SnO_2

The orthorhombic SnO_2 phase was reported to be a high-pressure phase that formed at 800 °C under a high pressure of ~1.2×10^8 torr.[120] It is, however, a surprise that the orthorhombic phase is found in the form of nanowires, sandwiched nanoribbons, and nanodendrites under the conditions of low temperature and low pressure as described above. The orthorhombic-structured SnO_2 nanowires and sandwiched nanoribbons were formed on a cold plate (its surface temperature is 25–60 °C) under a pressure of 200 torr using Sn foil/SnO mixture as source material. The orthorhombic nanodendrites were

synthesized at 200–400 °C and 500–600 torr using SnO powders. It was suggested that formation of the orthorhombic SnO_2 nanostructures might be caused by a deficiency in oxygen during the nanostructure growth. Our recent in-situ experiments prove that the orthorhombic SnO_2 phase can be formed by thermally decomposing SnO diskettes under high vacuum (<10^{-6} torr).[132] Figure 15a is a TEM image showing a part of a sub-branch of a nanodendrite, which has the orthorhombic
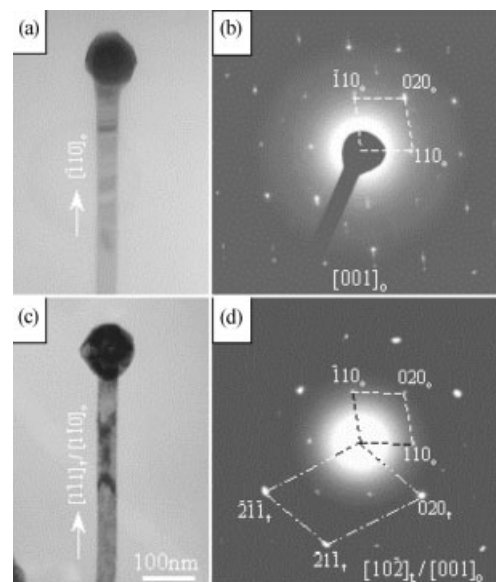

Fig. 15. a) TEM image of an orthorhombic SnO_2 nanowire with a Sn-rich head. b) Electron diffraction pattern corresponding to (a). The sample was made using SnO powders under 500–600 torr (argon) at 1050 °C and collected from the low-temperature region of 200–400 °C. c) TEM image of the orthorhombic SnO_2 nanowire undergoing annealing at 500 °C for 2 h in oxygen atmosphere. d) Electron diffraction pattern taken from the nanowire shown in (c).

structure. The corresponding electron diffraction pattern is shown in Figure 15b, which is the $[001]_o$ zone pattern of orthorhombic SnO_2. After post-annealing the sample at 500 °C for 2 h in an oxygen atmosphere, the morphology of the sub-branch looks similar to that before annealing (Fig. 15c). The corresponding electron diffraction pattern (Fig. 15d) is, however, different from that shown in Figure 15b. In comparison with the pattern of Figure 15b, some reflections are enhanced in intensity in Figure 15d, and they can be indexed as the $[10\bar{2}]_t$ zone of rutile-structured SnO_2. This implies that phase transformation from orthorhombic SnO_2 to rutile SnO_2 has occurred during the annealing. The weak reflections appearing in the pattern (Fig. 15d) indicate that the phase transformation is not completely finished under the current annealing conditions.

6. Growth Mechanism

6.1. Anisotropic Growth

Understanding the growth mechanism is critical in controlling and designing nanostructures. In the 1950s and 1960s, or

even earlier, it had been found in the study of whisker growth that acicular structured oxides of metals such as Cu, Cr, Fe, Pb, Ti, W, and Zn could be produced on the external surfaces of the corresponding metals when they were heated in air at certain temperatures.[133] Formation of the acicular oxides can be regarded as vapor–solid (VS) growth. Frank's dislocation growth mechanism[123] had been widely accepted for the growth of crystal whiskers, in which a screw dislocation with its Burgers' vector parallel to the growth direction provides self-perpetuating growth steps on the tip so that the tip is an efficient sink for adsorbing atoms. Blades (sheets) also appeared by oxidation of stressed materials in dry atmospheres.[134]

In the early 1960s, another crystal growth mechanism—vapor–liquid–solid (VLS)—was proposed by Wagner and Ellis[124] in their investigation of Si whisker growth. According to the VLS growth mechanism, the anisotropic crystal growth is guided by a droplet of liquid alloy. The droplet surface has a higher sticking coefficient and is therefore a preferred absorption site for incoming vapor reactant(s). As the liquid droplet becomes supersaturated with the vapor reactant(s), whisker growth will occur by means of a precipitation process of the reactant(s). The role of the droplet in the crystal growth process is analogous to a catalyst in a chemical reaction; VLS growth is also called catalysis growth. The whiskers grown by VLS usually have diameters in the micrometer range. On the basis of the VLS growth mechanism, a series of wire-like nanostructures have been synthesized for element semiconductors,[14] compound semiconductors,[16–18] and oxides such as ZnO,[37,38] SiO$_2$,[20,70–72] Ga$_2$O$_3$,[92,93,96] and In$_2$O$_3$.[88] Analogous to the VLS growth, a solution–liquid–solid (SLS) growth method was also developed recently to grow semiconductor nanowhiskers and nanowires at low temperature.[13,135]

Oxide-assisted growth is another mechanism proposed for nanowire formation in vapor growth.[15,136] This mechanism emphasizes that it is essential to form a thermodynamically unstable oxide phase. At low temperature, decomposition of the unstable oxide provides the nucleus for nanowire formation and the temperature gradient provides the driving force for nanowire growth.

6.2. Kinetics of Anisotropic Growth via the Vapor–Solid Mechanism

Recently, a variety of wire-like nanostructures of oxides, including nanowires,[32,54] nanorods,[22] and nanobelts,[26,53] have been produced by vapor growth methods without introducing any hetero-metal catalyst. The growth was likely governed by the VS process.[22,26] It is still an open question how the VS process can be responsible for the growth of wire-like nanostructures. Usually, the crystalline wire-like nanostructures are not cylindrical wires, but a faceted shape that consists of certain low-index crystallographic planes. Table 3 gives the crystallographic geometry of the oxide nanobelts and nanowires recently synthesized in our group. It seems that surface energy minimization may play an important role in formation of nanobelts and nanowires.[53] Minimizing the surface energy is, how-

ever, not sufficient for interpreting the formation of In$_2$O$_3$ and CdO nanobelts, both of which have cubic lattice structures and are enclosed by $\pm(100)$, $\pm(010)$, and $\pm(001)$ crystal planes, which are crystallographically equivalent. It may be argued that surface energy plays a key role in the formation of the nanobelt structure, but it has been found that amorphous silica can also form nanowire structures.[20,70–78] It is therefore implied that the formation of wire-like nanostructures might be controlled by kinetics during crystal growth. Much work has been done both experimentally and theoretically on the kinetics of whisker growth.[137–139] The two-dimensional (2D) nucleation probability on the surface of a whisker was established to be

$$P_N = B \exp\left(-\frac{\pi\sigma^2}{k^2 T^2 \ln \alpha}\right) \qquad (4)$$

where P_N is the nucleation probability, B a constant, σ the surface energy of the solid whisker; k the Boltzmann constant, T absolute temperature, and α the supersaturation ratio determined by $\alpha = p/p_0$ (usually $\alpha > 1$), where p is the actual vapor pressure and p_0 the equilibrium vapor pressure corresponding to temperature T. The surface energy is related to the crystal plane; a low-index crystal plane is of lower surface energy. According to Equation 4, the lower the surface energy, the larger the 2D nucleation probability. On the other hand, an atom adsorbed on a low-energy surface has low binding energy and a high probability of desorption.[140] Competition and coordination of the two processes are responsible for the formation of the low-index crystal planes enclosing the nanostructure. The temperature and the supersaturation ratio are two parameters controlled by processing conditions. Higher temperature and larger supersaturation ratio facilitate the 2D nucleation, resulting in the formation of the sheet-like structure. In contrast, lower temperature and smaller supersaturation ratio promote the growth of wire-like structures. Therefore, the temperature and the supersaturation ratio are two dominant processing factors in controlling the morphology of the product(s) in the VS growth process.

6.3. Growth Model of Oxide Nanobelts

To understand the growth of a uniform belt structure without the presence of hetero-catalysis particles, we propose a possible mechanism that may occur in nanobelt growth. The source material is assumed to vaporize into molecular species at high temperature, and the molecules are composed of stoichiometric cation–anion molecules, for instance ZnO (Fig. 16c). When condensed onto the substrate at a lower temperature region, the cation–anion molecules will be arranged in such a way that a proper cation–anion coordination is preserved to balance the local charge and structural symmetry (Fig. 16d), forming a small nucleus. Newly arriving molecules will continue to deposit on the formed nucleus while the surfaces that have lower energy start to form, such as the side surfaces. Because the growth temperature is in the range of 800–
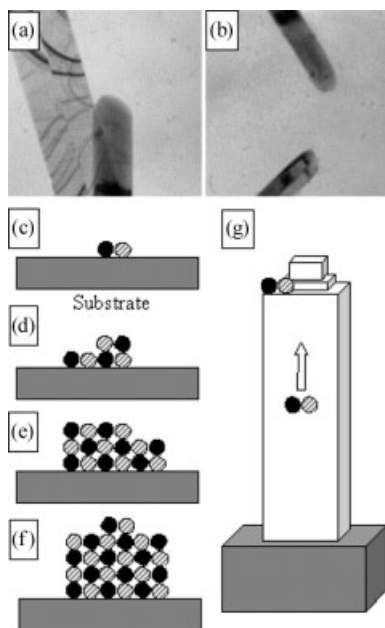
Fig. 16. a,b) The growth fronts/ends of ZnO nanobelts, showing no visible catalytic particles at the ends. c–g) A possible growth process for the formation of the nanobelt.

7. Nanodevices Based on Oxide Nanostructures

It is well known that carbon nanotubes hold major promise for nanoelectronics and nanointerconnects. The major barrier to application of carbon nanotubes is the control or selection of the tubes that are semiconducting from among metallic ones, because the semiconducting or metallic properties of the nanotubes depends on the helical angle with which the graphitic sheet is rolled up. Up to now no technique has been found to control the helical angle of the nanotubes. In contrast, the nanobelts of functional oxides that we have synthesized are intrinsic semiconductors and they have controlled morphology and structure. This offers a huge advantage over carbon nanotubes for application in nanoelectronics. Recently, field effect transistors (FETs) constructed using a single ZnO nanobelt have been made by placing a nanobelt onto the Au electrodes mounted on a semiconductor Si chip.[141] Figure 17 shows a current–voltage (*I–V*) curve of a FET built using a single ZnO nanobelt. Controlling the back gate voltage has demonstrated

1000 °C, the mobility of the atoms/molecules is high enough that the low-energy surfaces tend to be flat, thus preventing the accumulation of newly arriving molecules on the surface, resulting in its expansion in surface area as more molecules stick onto the rough growth front (Fig. 16e). The rough structure of the tip leads to a rapid accumulation of incoming molecules, resulting in the fast formation of a nanobelt (Fig. 16f), and after some time a long nanobelt is formed (Fig. 16g). Figures 16a and 16b show tips of ZnO nanobelts, in which the growth fronts are a rounded shape, indicating their atomic-scale roughness with the presence of steps, ledges, and kinks. The newly arrived molecules can continue to stick onto the growth front, or the side surfaces, but the smooth side surface and the high molecular mobility at the growth temperature prevent them remaining on the surface, and the molecules will randomly diffuse on the surface and finally find the lower energy sites at the growth front. The molecules are unlikely to stick to the edge of the nanobelts because of the unbalanced coordination and possibly higher energy. The size of the nanobelt cross section is determined by the growth temperature and supersaturation ratio in the kinetics of crystal growth, as mentioned above.

We still cannot completely rule out the possibility of self-catalyzed growth, in which a small thin—even atomically "thin"—metal layer, for example of Zn, is present at the growth front, which could lead to growth via VLS. The layer could be quickly oxidized after the nanobelts are exposed to air after the growth, and our ex-situ analysis may never find this layer. The self-catalyzed growth was, however, indeed observed in the Sn–O system, which was adopted by some product formed in the low-temperature region (Fig. 10).
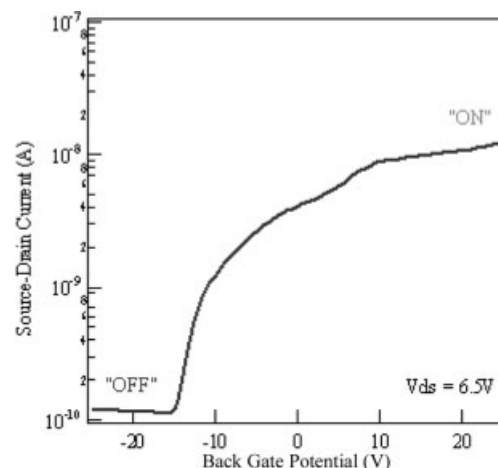

Fig. 17. The source–drain current measured for a field effect transistor built based on a single ZnO nanobelt as a function of the back gate voltage, showing the "ON" and "OFF" modes of the transistor [141].

switching ratios as large as six orders of magnitude, conductivity as high as $10 \ \Omega^{-1} \ cm^{-1}$, and mobility as large as $35 \ cm^2 \ V^{-1} \ s^{-1}$. It has been found that metallic and semiconductive SnO_2 nanobelts can be created by annealing the nanobelts in vacuum to induce oxygen deficiency, resulting in property-controlled FET devices.[141] It is an important characteristic of functional oxides that controlling oxygen vacancies results in tunable electric properties.

It has been shown that the FET is very sensitive to UV (ultraviolet) illumination,[141] and, in turn, the device can be controlled by UV illumination. In ZnO nanobelts, which have a direct bandgap in the UV region, two processes are observed to contribute to photoconductivity. The first process is due to the photons generating electron–hole pairs, and the second process is most likely due to desorption of oxygen from the ZnO surface on exposure to UV.

The semiconducting properties of the nanobelts make it possible to build nano-sized sensors using individual nanobelts. Gas sensors based on two-electrode contact have been fabricated using a single-crystalline SnO_2 nanobelt.[142] The conductance of the nanobelt is affected by the surface-adsorbed molecules, resulting in a sharp change in the electric current. Electrical characterization showed that the contacts were ohmic and the nanobelts were sensitive to environmental polluting species such as CO and NO_2 as well as ethanol for breath analyzers and food control applications. The sensor response, defined as the relative variation in conductance due to the introduction of the gas, is $\Delta G/G = 200\,\%$ for 250 ppm of ethanol and $\Delta G/G = -3000\,\%$ for 0.5 ppm nitrogen dioxide at 200 °C (Fig. 18). The sensor displays selectivity between ethanol and NO_2. The results demonstrate the potential of fabricating nano-sized sensors using the integrity of a single nanobelt with sensitivity at the level of a few parts per billion [ppb]. Beyond conventional gas and chemical sensors, nano-sized sensors may be applicable as biosensors for biomedical applications.
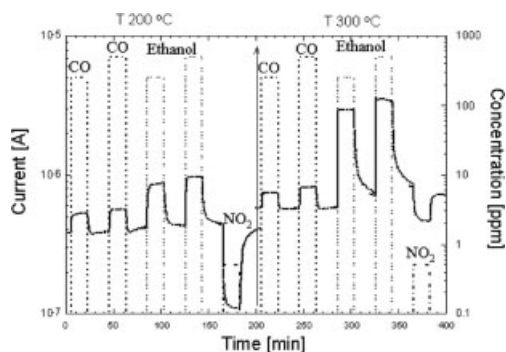

Fig. 18. Response of SnO_2 sensors to CO, ethanol, and NO_2 gases at 200 °C (left) and 300 °C (right) at different gas concentrations. The scale for the electric current (continuous line) is given at the left and that for the gas concentration in parts per million [ppm] at the right [142].

8. Concluding Remarks and Perspectives

This article reviews the novel nanostructures of functional oxides, including nanobelts, nanowires, nanosheets, and nanodiskettes, which have been synthesized in our laboratory. Among the group of ZnO, SnO_2, In_2O_3, Ga_2O_3, CdO, and PbO_2, which belong to different crystallographic systems and structures, a generic nanobelt structure has been synthesized. The nanobelts are single crystalline and dislocation-free, and their surfaces are atomically flat. The oxides are intrinsic semiconductors and have been used for fabrication of nano-sized functional devices, such as field effect transistors and gas sensors. Taking SnO_2 and SnO as examples, other types of novel nanostructures have also been illustrated and discussed. Their growth, phase transformation, and stability are considered.

The nanobelts and related nanostructures are a unique group that is likely to have important applications in nano-sized electronic, optical, sensor and optoelectronic devices. Considering the future of nanotechnology, a great many issues remain to be investigated:

- Under the presupposition of preserving high quality and freedom from dislocations, the development of low-temperature techniques to synthesize oxide nanostructures will be important for integration with silicon-based microelectronics and for decreasing cost of fabrication. Lowering of the synthesis temperature in thermal evaporation will be possible with the aid of carbon-thermal[22] and hydrogen-thermal[82] processes, or by replacing the oxide powders by the corresponding metal–organic compounds as source materials.[44]

- Our experiments show that control of the pressure, growth temperature, and gradient is critical in controlling morphology and phase structure of the growth products, especially for the nanostructures of the Sn–O system. Development of techniques in this direction is, therefore, important for industrialization of the synthesis process.

- Oxygen vacancy defects are hard to avoid in the synthesis of oxide nanostructures, resulting in the formation of non-stoichiometric phase structures. On the other hand, the existence of the oxygen vacancies makes the properties of the oxide nanostructures tunable. How to control the distribution of the oxygen vacancies over the oxide nanostructures and understanding the relationship between the oxygen vacancies and properties of the nanostructures are, however, still fundamental issues that need to be investigated.

- The as-synthesized functional oxides are intrinsic semiconductors, but their conductivity and functionality depend on doping. Techniques are needed for controlling the doping process and the doping concentration. For the nanostructures that we presented here, it is not clear if the dopant elements are located on the surface or in the volume.

- For sensor applications, the nanobelts may have the required sensitivity, but the selectivity needs to be improved. This requires the synthesis of composite nanobelts, such as heterostructures, junctions, and barriers. Exploration of complex oxides involving two or more types of cations is needed to improve their multifunctionality. Surface functionalization of the nanobelts is also an important direction.

- Controlled growth is required to control their size, size distribution, shape, crystal structure, defect distribution, and even surface structure (atomic termination, surface polarization). A thorough understanding of the growth mechanism(s) is the key. In processing, a valid way to control the size of the nanobelts is to properly control the temperature, pressure, and growth time.

- Techniques are required to grow the nanobelts into aligned arrays, onto patterned substrates, and in self-assembling structures with functionality. Aligned arrays of ZnO nanowires have been fabricated,[38,39,44] and it was suggested that the nanowires can function as natural resonance cavities.

- Finally, development of techniques for integration of nanobelts with other nano- and microstructures, such as microelectromechanical systems (MEMS) and silicon-based technology, are critical for future applications.

[1] C. M. Lieber, *Solid State Commun.* **1998**, *107*, 607.
[2] H. Gleiter, *Acta Mater.* **2000**, *48*, 1.
[3] S. Iijima, *Nature* **1991**, *354*, 56.
[4] N. G. Chopra, R. J. Luyken, K. Cherrey, V. H. Crespi, M. L. Cohen, S. G. Louie, A. Zettl, *Science* **1995**, *269*, 966.
[5] E. Bengu, L. D. Marks, *Phys. Rev. Lett.* **2001**, *86*, 2385.
[6] A. Rothschild, J. Sloan, R. Tenne, *J. Am. Chem. Soc.* **2000**, *122*, 5169.
[7] F. Krumeich, H. J. Muhr, M. Niederberger, F. Bieri, B. Schnyder, R. Nesper, *J. Am. Chem. Soc.* **1999**, *121*, 8324.
[8] M. Remskar, A. Mrzel, Z. Skraba, A. Jesih, M. Ceh, J. Demsar, P. Stadelmann, F. Levy, D. Mihailovic, *Science* **2001**, *292*, 479.
[9] B. C. Satishkumar, A. Govindaraj, E. M. Vogl, L. Basumallick, C. N. R. Rao, *J. Mater. Res.* **1997**, *12*, 604.
[10] M. Adachi, T. Harada, M. Harada, *Langmuir* **1999**, *15*, 7097.
[11] R. Tenne, M. Homyonfer, Y. Feldman, *Chem. Mater.* **1998**, *10*, 3225.
[12] Y. Saito, T. Matsumoto, *Nature* **1998**, *392*, 237.
[13] T. J. Trentler, K. M. Hickman, S. C. Goel, A. M. Viano, P. C. Gibbons, W. E. Buhro, *Science* **1995**, *270*, 1791.
[14] A. M. Morales, C. M. Lieber, *Science* **1998**, *279*, 208.
[15] S. T. Lee, N. Wang, Y. F. Zhang, Y. H. Tang, *MRS Bull.* **1999**, *24*, 36.
[16] X. F. Duan, C. M. Lieber, *Adv. Mater.* **2000**, *12*, 298.
[17] C. C. Chen, C. C. Yeh, C. H. Chen, M. Y. Yu, H. L. Liu, J. J. Wu, K. H. Chen, L. C. Chen, J. Y. Peng, Y. F. Chen, *J. Am. Chem. Soc.* **2001**, *123*, 2791.
[18] M. H. Huang, Y. Y. Wu, H. Feick, N. Tran, E. Weber, P. D. Yang, *Adv. Mater.* **2001**, *13*, 113.
[19] M. J. Zheng, L. D. Zhang, X. Y. Zhang, J. Zhang, G. H. Li, *Chem. Phys. Lett.* **2001**, *334*, 298.
[20] Z. W. Pan, Z. R. Dai, C. Ma, Z. L. Wang, *J. Am. Chem. Soc.* **2002**, *124*, 1817.
[21] H. J. Dai, E. W. Wong, Y. Z. Lu, S. S. Fan, C. M. Lieber, *Nature* **1995**, *375*, 769.
[22] P. D. Yang, C. M. Lieber, *J. Mater. Res.* **1997**, *12*, 2981.
[23] L. Manna, E. C. Scher, A. P. Alivisatos, *J. Am. Chem. Soc.* **2000**, *122*, 12 700.
[24] Y. Zhang, K. Suenaga, C. Colliex, S. Iijima, *Science* **1998**, *281*, 973.
[25] Z. L. Wang, Z. R. Dai, R. P. Gao, Z. G. Bai, J. L. Gole, *Appl. Phys. Lett.* **2000**, *77*, 3349.
[26] Z. W. Pan, Z. R. Dai, Z. L. Wang, *Science* **2001**, *291*, 1947.
[27] W. Shi, H. Peng, N. Wang, C. P. Li, L. Xu, C. S. Lee, R. Kalish, S. T. Lee, *J. Am. Chem. Soc.* **2001**, *123*, 11 095.
[28] Z. R. Dai, Z. W. Pan, Z. L. Wang, *J. Phys. Chem. B* **2002**, *106*, 902.
[29] Z. R. Dai, Z. W. Pan, Z. L. Wang, *J. Am. Chem. Soc.* **2002**, *124*, 8673.
[30] Z. L. Wang, Z. C. Kang, *Functional and Smart Materials*, Plenum, New York **1998**.
[31] Z. W. Pan, Z. R. Dai, Z. L. Wang, *Appl. Phys. Lett.* **2001**, *80*, 309.
[32] Y. Yin, G. Zhang, Y. Xia, *Adv. Funct. Mater.* **2002**, *12*, 293.
[33] C. Tang, Y. Bando, T. Sato, *J. Phys. Chem. B* **2002**, *106*, 7449.
[34] Y. Li, Y. Bando, T. Sato, *Chem. Phys. Lett.* **2002**, *359*, 141.
[35] Y. Q. Zhu, W. K. Hsu, W. Z. Zhou, M. Terrones, H. W. Kroto, D. R. M. Walton, *Chem. Phys. Lett.* **2001**, *347*, 337.
[36] B. D. Bao, Y. F. Chen, N. Wang, *Appl. Phys. Lett.* **2002**, *81*, 757.
[37] M. H. Huang, S. Mao, H. Feick, H. Yan, Y. Wu, H. Kind, E. Weber, R. Russo, P. Yang, *Science* **2001**, *292*, 1897.
[38] M. H. Huang, Y. Wu, H. Feick, N. Tran, E. Weber, P. Yang, *Adv. Mater.* **2001**, *13*, 113.
[39] P. Yang, H. Yan, S. Mao, R. Russo, J. Johnson, R. Saykally, N. Morris, J. Pham, R. He, H. J. Choi, *Adv. Funct. Mater.* **2002**, *12*, 323.
[40] Y. C. Kong, D. P. Yu, B. Zhang, W. Feng, S. Q. Feng, *Appl. Phys. Lett.* **2001**, *78*, 407.
[41] Y. W. Wang, L. D. Zhang, G. Z. Wang, X. S. Peng, Z. Q. Chu, C. H. Liang, *J. Cryst. Growth* **2002**, *234*, 171.
[42] Y. Dai, Y. Zhang, Q. K. Li, C. W. Nan, *Chem. Phys. Lett.* **2002**, *358*, 83.
[43] J. Y. Li, X. L. Chen, H. Li, M. He, Z. Y. Qiao, *J. Cryst. Growth* **2001**, *233*, 5.
[44] W. I. Park, D. H. Kim, S. W. Jung, G. C. Yi, *Appl. Phys. Lett.* **2002**, *80*, 4232.
[45] J. J. Wu, S. C. Liu, *Adv. Mater.* **2002**, *14*, 215.
[46] C. Xu, G. Xu, Y. Liu, G. Wang, *Solid State Commun.* **2002**, *122*, 175.
[47] L. Guo, J. X. Cheng, X. Y. Li, Y. J. Yan, S. H. Yang, C. L. Yang, J. N. Wang, *Mater. Sci. Eng. C* **2001**, *16*, 123.
[48] J. Q. Hu, Q. Li, N. B. Wong, C. S. Lee, S. T. Lee, *Chem. Mater.* **2002**, *14*, 1216.
[49] J. Zhang, L. Sun, C. Liao, C. Yan, *Chem. Commun.* **2002**, 262.
[50] L. Vayssieres, K. Keis, A. Hagfeldt, S. E. Lindquist, *Chem. Mater.* **2001**, *13*, 4395.
[51] Y. Liu, C. Yin, W. Wang, Y. Zhan, G. Wang, *J. Mater. Sci. Lett.* **2002**, *21*, 137.
[52] X. L. Xu, D. P. Yu, S. Q. Feng, X. F. Duan, Z. Zhang, *Nanostruct. Mater.* **1997**, *8*, 373.
[53] Z. R. Dai, Z. W. Pan, Z. L. Wang, *Solid State Commun.* **2001**, *118*, 351.
[54] Z. R. Dai, J. L. Gole, J. D. Stout, Z. L. Wang, *J. Phys. Chem. B* **2002**, *106*, 1274.
[55] J. Q. Hu, X. L. Ma, N. G. Shang, Z. Y. Xie, N. B. Wong, C. S. Lee, S. T. Lee, *J. Phys. Chem. B* **2002**, *106*, 3823.
[56] Y. Liu, C. Zheng, W. Wang, C. Yin, G. Wang, *Adv. Mater.* **2001**, *13*, 1883.
[57] S. J. Limmer, S. Seraji, Y. Wu, T. P. Chou, C. Nguyen, G. Cao, *Adv. Funct. Mater.* **2002**, *12*, 59.
[58] Z. G. Bai, D. P. Yu, H. Z. Zhang, Y. P. Wang, X. Z. Gai, Q. L. Hang, G. C. Xiong, S. Q. Feng, *Chem. Phys. Lett.* **1999**, *303*, 311.
[59] Y. Zhang, J. Zhu, Q. Zhang, Y. Yan, N. Wang, X. Zhang, *Chem. Phys. Lett.* **2000**, *317*, 504.
[60] Y. H. Tang, Y. F. Zhang, N. Wang, I. Bello, C. S. Lee, S. T. Lee, *Appl. Phys. Lett.* **1999**, *74*, 3824.
[61] S. Aggarwal, A. P. Monga, S. R. Perusse, R. Ramesh, V. Ballarotto, E. D. Williams, B. R. Chalamala, Y. Wei, R. H. Reuss, *Science* **2000**, *287*, 2235.
[62] Y. Lei, L. D. Zhang, G. W. Meng, G. H. Li, X. Y. Zhang, C. H. Liang, W. Chen, S. X. Wang, *Appl. Phys. Lett.* **2001**, *78*, 1125.
[63] Z. Miao, D. Xu, J. Ouyang, G. Guo, X. Zhao, Y. Tang, *Nano Lett.* **2002**, *2*, 717.
[64] J. H. Jung, H. Kobayashi, K. J. C. van Bommel, S. Shinkai, T. Shimizu, *Chem. Mater.* **2002**, *14*, 1445.
[65] D. Gong, C. A. Grimes, O. K. Varghese, W. Hu, R. S. Singh, Z. Chen, E. C. Dickey, *J. Mater. Res.* **2001**, *16*, 3331.
[66] G. H. Du, Q. Chen, R. C. Che, Z. Y. Yuan, L. M. Peng, *Appl. Phys. Lett.* **2001**, *79*, 3702.
[67] S. Kobayashi, K. Hanabusa, N. Hamasaki, M. Kimura, H. Shirai, S. Shinkai, *Chem. Mater.* **2000**, *12*, 1523.
[68] T. Sasaki, Y. Ebina, Y. Kitami, M. Watanabe, T. Oikawa, *J. Phys. Chem. B* **2001**, *105*, 6116.
[69] S. Kobayashi, N. Hamasaki, M. Suzuki, M. Kimura, H. Shirai, K. Hanabusa, *J. Am. Chem. Soc.* **2000**, *124*, 6550.
[70] D. P. Yu, Y. J. Xing, Q. L. Hang, H. F. Yan, J. Xu, Z. H. Xi, S. Q Feng, *Physica E* **2001**, *9*, 305.
[71] H. F. Yan, Y. J. Xing, Q. L. Hang, D. P. Yu, Y. P. Wang, J. Xu, Z. H. Xi, S. Q. Feng, *Chem. Phys. Lett.* **2000**, *323*, 224.
[72] B. Zhang, Y. Wu, P Yang, J. Liu, *Adv. Mater.* **2002**, *14*, 122.
[73] S. Jin, Q. Li, C. S. Lee, *Phys. Status Solidi A* **2001**, *188*, R1.
[74] Y. J. Chen, J. B. Li, Y. S. Han, Q. M. Wei, J. H. Dai, *Appl. Phys. A* **2002**, *74*, 433.
[75] Y. W. Wang, C. H. Liang, G. W. Meng, X. S. Peng, L. D. Zhang, *J. Mater. Chem.* **2002**, *12*, 651.
[76] C. H. Liang, L. D. Zhang, G. W. Meng, Y. W. Wang, Z. Q. Chu, *J. Non-Cryst. Solids* **2000**, *277*, 63.
[77] Z. L. Wang, R. P. Gao, J. L. Gole, J. D. Stout, *Adv. Mater.* **2000**, *12*, 1938.
[78] Y. J. Chen, J. B. Li, Y. S. Han, J. H. Dai, *J. Mater. Sci. Lett.* **2002**, *21*, 175.
[79] L. Wang, S. Tomura, F. Ohashi, M. Maeda, M. Suzuki, K. Inukai, *J. Mater. Chem.* **2001**, *11*, 1465.
[80] Y. Ono, K. Nakashima, M. Sano, J. Hojo, S. Shinkai, *J. Mater. Chem.* **2001**, *11*, 2412.
[81] J. H. Jung, Y. Ono, K. Hanabusa, S. Shinkai, *J. Am. Chem. Soc.* **2000**, *122*, 5008.
[82] X. Wang, Y. Li, *J. Am. Chem. Soc.* **2002**, *124*, 2880.
[83] X. Wang, Y. Li, *Chem. Commun.* **2002**, 764.
[84] W. Wang, C. Xu, G. Wang, Y. Liu, C. Zheng, *Adv. Mater.* **2002**, *14*, 837.
[85] C. N. R. Rao, B. C. Satishkumar, A. Govindaraj, *Chem. Commun.* **1997**, 1581.
[86] J. Bao, C. Tie, Z. Xu, Q. Ma, J. Hong, H. Sang, D. Sheng, *Adv. Mater.* **2002**, *14*, 44.
[87] X. S. Peng, Y. W. Wang, J. Zhang, X. F. Wang, L. X. Zhao, G. W. Meng, L. D. Zhang, *Appl. Phys. A* **2002**, *74*, 437.
[88] C. Liang, G. Meng, Y. Lei, F. Phillipp, L. Zhang, *Adv. Mater.* **2001**, *13*, 1330.
[89] H. Yumoto, T. Sako, Y. Gotoh, K. Nishiyama, T. Kaneko, *J. Cryst. Growth* **1999**, *203*, 136.
[90] J. Zhang, L. Zhang, *Solid State Commun.* **2002**, *122*, 493.
[91] G. Gundiah, A. Govindaraj, C. N. R. Rao, *Chem. Phys. Lett.* **2002**, *351*, 189.
[92] Y. C. Choi, W. S. Kim, Y. S. Park, S. M. Lee, D. J. Bae, Y. H. Lee, G. S. Park, W. B. Choi, N. S. Lee, J. M. Kim, *Adv. Mater.* **2000**, *12*, 746.
[93] G. S. Park, W. B. Choi, J. M. Kim, Y. C. Choi, Y. H. Lee, C. B. Lim, *J. Cryst. Growth* **2002**, *220*, 494.
[94] X. C. Wu, W. H. Song, W. D. Huang, M. H. Pu, B. Zhao, Y. P. Sun, J. J. Du, *Chem. Phys. Lett.* **2000**, *328*, 5.
[95] H. Z. Zhang, Y. C. Kong, Y. Z. Wang, X. Du, Z. G. Bai, J. J. Wang, D. P. Yu, Y. Ding, Q. L. Hang, S. Q. Feng, *Solid State Commun.* **1999**, *109*, 677.
[96] W. Q. Han, P. Kohler-Redlich, F. Ernst, M. Rühle, *Solid State Commun.* **2000**, *115*, 527.
[97] H. J. Muhr, F. Krumeich, U. P. Schönholzer, F. B. Markus, M. Niederberger, L. J. Gauckler, R. Nesper, *Adv. Mater.* **2000**, *12*, 231.

[98] F. Krumeich, H. J. Muhr, M. Niederberger, F. Bieri, R. Nesper, *Z. Anorg. Allg. Chem.* **2000**, *626*, 2208.

[99] A. Dobley, K. Ngala, S. Yang, P. Y. Zavalij, M. S. Whittingham, *Chem. Mater.* **2001**, *13*, 4382.

[100] P. Millet, J. Y. Henry, F. Mila, J. Galy, *J. Solid State Chem.* **1999**, *147*, 676.

[101] J. Choi, J. L. Musfeldt, Y. J. Wang, H. J. Koo, M. H. Whangbo, J. Galy, P. Millet, *Chem. Mater.* **2002**, *14*, 924.

[102] Y. Fu, J. Chen, H. Zhang, *Chem. Phys. Lett.* **2001**, *350*, 491.

[103] L. Vayssieres, N. Beermann, S. E. Lindquist, A. Hagfeldt, *Chem. Mater.* **2001**, *13*, 233.

[104] W. Wang, G. Wang, X. Wang, Y. Zhan, Y. Liu, C. Zhang, *Adv. Mater.* **2002**, *14*, 67.

[105] L. Huang, H. Wang, Z. Wang, A. Mitra, D. Zhao, Y. Yan, *Chem. Mater.* **2002**, *14*, 876.

[106] B. C. Satishkumar, A. Govindaraj, M. Nath, C. N. R. Rao, *J. Mater. Chem.* **2000**, *10*, 2115.

[107] G. Gu, B. Aheng, W. Q. Han, S. Roth, J. Liu, *Nano Lett.* **2002**, *2*, 849.

[108] M. Yada, M. Mihara, S. Mouri, M. Kuroki, T. Kijima, *Adv. Mater.* **2002**, *14*, 309.

[109] J. J. Urban, W. S. Yun, Q. Gu, H. Park, *J. Am. Chem. Soc.* **2002**, *124*, 1186.

[110] B. A. Hernandez, K. S. Chang, E. R. Fisher, P. K. Dorhout, *Chem. Mater.* **2002**, *14*, 480.

[111] S. J. Limmer, S. Seraji, M. J. Forbess, Y. Wu, T. P. Chou, C. Nguyen, G. Cao, *Adv. Mater.* **2001**, *13*, 1269.

[112] R. Jayavel, T. Mochiku, S. Ooi, K. Hirata, *J. Cryst. Growth* **2001**, *229*, 339.

[113] L. Brewer, *Chem. Rev.* **1953**, *52*, 1.

[114] G. L. Humphrey, C. J. O'Brien, *J. Am. Chem. Soc.* **1953**, *75*, 2805.

[115] T. Y. Tan, S. T. Lee, U. Gösele, *Appl. Phys. A* **2002**, *74*, 423.

[116] C. L. Hoenig, A. W. Searcy, *J. Am. Ceram. Soc.* **1966**, *49*, 128.

[117] K. K. Kelley, *U.S. Bur. Mines Bull.* **1949**, *476*, 187.

[118] D. S. Ginley, C. Bright, *MRS Bull.* **2000**, *25*, 15.

[119] W. H. Baou, *Acta Crystallogr.* **1956**, *9*, 515.

[120] K. Suito, N. Kawai, Y. Masuda, *Mater. Res. Bull.* **1975**, *10*, 677.

[121] S. Geller, *J. Chem. Phys.* **1960**, *33*, 676.

[122] W. J. Moore, L. Pauling, *J. Am. Chem. Soc.* **1941**, *63*, 1392.

[123] F. C. Frank, *Discuss. Faraday Soc.* **1949**, *5*, 48.

[124] R. S. Wagner, W. C. Ellis, *Appl. Phys. Lett.* **1964**, *4*, 89.

[125] H. Harada, *J. Appl. Crystallogr.* **1981**, *14*, 141.

[126] J. Leciejewicz, *Acta Crystallogr.* **1961**, *14*, 1340.

[127] V. T. Deshpande, D. B. Sirdeshmukh, *Acta Crystallogr.* **1961**, *14*, 355.

[128] F. Lawson, *Nature* **1967**, *215*, 955.

[129] J. P. Coughlin, *U.S. Bur. Mines Bull.* **1953**, *542*, 51.

[130] G. Murken, M. Trömel, *Z. Anorg. Allg. Chem.* **1973**, *397*, 117.

[131] *JCPDS (International Center for Diffraction Data)*, **1997**, 18-1386.

[132] Z. R. Dai, Z. W. Pan, Z. L. Wang, unpublished.

[133] S. M. Arnold, S. E. Kounce, *J. Appl. Phys.* **1956**, *27*, 964.

[134] R. A. Ploc, *Ph.D. Thesis*, University of Cambridge, UK **1965**.

[135] J. D. Holmes, K. P. Johnston, R. C. Doty, B. A. Korgel, *Science* **2000**, *287*, 1471.

[136] N. Wang, Y. H. Tang, Y. F. Zhang, C. S. Lee, I. Bello, S. T. Lee, *Chem. Phys. Lett.* **1999**, *299*, 237.

[137] N. Cabrera, W. K. Burton, *Discuss. Faraday Soc.* **1949**, *5*, 40.

[138] G. W. Sears, *Acta Metall.* **1955**, *3*, 361.

[139] J. M. Blakely, K. A. Jackson, *J. Chem. Phys.* **1962**, *37*, 428.

[140] B. Lewis, in *Crystal Growth* (Ed: B. R. Pamplin), Pergamon, Oxford **1980**, pp. 23–63.

[141] M. S. Arnold, P. Avouris, Z. L. Wang, *J. Phys. Chem B*, in press.

[142] E. Comini, G. Faglia, G. Sberveglieri, Z. W. Pan, Z. L. Wang, *Appl. Phys. Lett.* **2002**, *81*, 1869.

_____